RESEARCH ARTICLE

Unravelling the Ageing Effects of PDMS-Based Triboelectric Nanogenerators

Tianhuai Xu, Jiahao Ye, and Jin-Chong Tan*

Ageing of elastomeric materials in triboelectric nanogenerators (TENGs) often leads to compromised electrical performance and can greatly affect their real-world application as next-generation energy harvesters and self-powered sensors. Herein, the ageing behavior of PDMS-based TENGs is investigated by probing the dielectric and mechanical properties of the membrane materials. Over time, ageing of PDMS after 17 months is evinced by a decline by 71%, 68% and 52% in open-circuit voltage, short-circuit current and charge transfer, respectively, and an increase by 6.8 times in surface charge decay rate. The reduced electrical performance can be attributed to a decrease in work function, dielectric constant, surface adhesion and heterogeneity in stiffness, as well as an increase in loss tangent. The effect of chemical chain scission on the PDMS surface is confirmed through nearfield infrared nanospectroscopy. This study gives insights into the underlying mechanism behind the ageing of PDMS-based TENGs, paving the way to future work for ameliorating these ageing-related issues with the aim to ensure long-term stability of practical triboelectric devices.

1. Introduction

Polydimethylsiloxane (PDMS) is a silicone-based elastomer that is composed of repeating units of $[SiO(CH_3)_2]$ monomers linked by the siloxane (Si—O—Si) groups.[1] Due to its excellent electron-withdrawing ability, PDMS has been widely adopted as a negative triboelectrification material in triboelectric nanogenerators (TENGs), which are energy transducers that convert oscillatory mechanical motions into electrical power.[2] Applications of PDMS-based TENGs have been explored in a variety of promising fields, such as power generation,[3,4] wearable self-powered devices and sensors,[5–7] Internet of Things,[8] and tactile e-skins for soft robotics.[9–12] The flexibility, stretchability, and

mechanical resilience of PDMS elastomers enable its easy adaptation to a myriad of potential TENG applications and composites, while maintaining a reasonably high power output density ranging from ca. 1–10s W m^{-2}.[3,13,14] In 2019, Kang et al. introduced conducting hierarchical wrinkles on the PDMS surface and successfully constructed a TENG-based electronic skin (e-skin).[11] The proposed e-skin took advantage of the stretchability and adaptability of PDMS and was employed as a pressure sensor with a sensitivity of 1.187 mV Pa^{-1}. In 2021, Sun et al. developed a self-powered tactile sensing and smart control system from a PDMS-based TENG device.[12] By incorporating graphite fillers and inducing microstructures on the PDMS surface, they reported a high-pressure sensitivity of 7.3 V Pa^{-1}. Later in 2022, Zhang et al. adopted a 3D TENG configuration and fabricated a self-powered force sensor that can detect multidimensional forces.[9] By molding PDMS into the desired cone-shape sensing structure, they achieved a normal force sensitivity of 2.97 mV kPa^{-1} and can easily recognize the force direction from the signals. Likewise, Li et al. reported a wearable PDMS-based TENG device for movement monitoring during exercise.[6] Due to the strong hydrophobicity and self-cleaning nature of PDMS, they demonstrated that the device exhibits superior humidity and contamination resistance and shows good performance stability before and after sweating.

Over the years, substantial effort has been put into developing strategies to enhance the electrical output of PDMS-based TENGs, including surface texturing,[4,15] surface functionalization,[16] ion injection,[17] and incorporation of fillers.[3,5,12] Such strategies can either induce more charge generation on the surface or add charge traps within the material for better charge storage.[18] However, limited research has been focused on the ageing effect of polymeric materials and how this might affect the durability of the TENG devices derived from elastomers such as PDMS. For mechanically robust and chemically stable polymers such as PTFE (polytetrafluoroethylene) and FEP (fluorinated ethylenepropylene), ageing has become less of a concern since these stiffer polymers can usually maintain their mechanical properties and do not degrade rapidly with time. However, soft elastomers like PDMS often suffer from poorer performance stability due to the evolution of their chemical and mechanical properties from ageing effects. As a matter of

T. Xu, J. Ye, J.-C. Tan
Multifunctional Materials & Composites (MMC) Laboratory
Department of Engineering Science
University of Oxford
Parks Road, Oxford OX1 3PJ, UK
E-mail: jin-chong.tan@eng.ox.ac.uk

**ADVANCED
SCIENCE NEWS**

www.advancedsciencenews.com

**ADVANCED
MATERIALS
INTERFACES**

www.advmatinterfaces.de

fact, ageing of materials can be catastrophic to the real-world application of PDMS-based TENGs.[19] For instance, when applied in an energy generation device, aged elastomers often lead to a compromised electrical output, thus lowering the energy harvesting efficiency of TENG. On the other hand, if used as a pressure sensor, ageing demands regular recalibration of the device, as the unstable signal output would affect reliability in long-term operations.

In this work, the electrical output, maximum surface charge density (MSCD) and surface charge decay were investigated to demonstrate how ageing can affect the charge generation and trapping ability of PDMS-based TENG devices. The changes in material properties with ageing were dissected from both the physical and chemical perspectives. The dielectric and mechanical properties, as well as the work function and chemical decomposition of PDMS, were analyzed using micro- and nanoscale characterization techniques and the results revealed the underpinning mechanisms responsible for the difference in TENG output performance.

2. Results and Discussion

2.1. TENG Performance Characterization

The working principle of the conductor-to-dielectric contact-separation mode TENG is depicted in **Figure** 1a. The PDMS film acts as the tribo-negative material (top) and is paired with a copper sheet (bottom), which functions as both a charge donor (tribo-positive material) and an electrode. Before the two tribo-electric layers were put into contact, no charge transfer occurs between the two electrodes. After the two materials are compressed together, charge forms at the interface due to contact electrification. PDMS with higher electron affinity carries negative charges, while copper on the other side bears charges of equal amount but of an opposite polarity. Upon films separation, electrons start to flow from the top electrode to the bottom one as a potential difference emerges from electrostatic induction. Electron flow stops when charge equilibrium is reached on both triboelectric layers and maximum potential is achieved between the two electrodes at full separation. When the two films are brought into contact again, electric potential drops, which consequently drives the electrons to flow back to the top electrode.

The charge generation capability of the samples was compared by measuring the open-circuit voltage, closed-circuit current and transferred charge in each tapping (contact-separation) cycle, as illustrated in Figure 1b–d. It is clear that with ageing, the electrical performance of PDMS-based TENG declines significantly. The highest electrical output was obtained for the pristine PDMS film (3×3 cm^2) with an open-circuit voltage of 232 V, a short-circuit current of 6 µA and a charge transfer of 18 nC per tapping. However, for the film that was aged for 6 months, the voltage output decreased by around 21%, the current output dropped 30% and the charge transfer declined by 17%. The 17 month old PDMS film exhibited even poorer electrical performance, with voltage, current and charge transfer output dropping by 71%, 68%, and 52% compared to the pristine PDMS film, respectively.

The charge trapping ability was further investigated through an ion injection test, and the effect of ion injection was stud-

ied on the TENG setup. An antistatic gun was employed to constantly inject negative ions onto the PDMS surface until the maximum surface charge density was reached. It is determined from the electrometer that each injection roughly induces the same amount of charge transfer (24.5 ± 5.6 nC) (Figure S5, Supporting Information). After each injection, the negatively biased film was brought into contact-separation mode with Cu and the short-circuit charge transfer generated by the TENG structure was recorded, which indicates the charge amount retained on the film surface. Figure 1e shows the transfer of induced charges on the pristine PDMS film before and after injection. Initially, before any negative ions were introduced, the obtained surface static charge on PDMS was purely induced by the triboelectrification with Cu. After the first injection, the output charge transfer suddenly jumped to a relatively high level of above 30 nC, and then each subsequent injection only resulted in a small elevation in surface charge until a decrease in charge was observed after the fourth injection. Such an abrupt decline can be explained by the air breakdown effect, where the electric potential across the air gap induced by electrostatic induction exceeds the maximum voltage the air can withstand.[20] Above this threshold value, the corona discharge of air will generate positive ions that can partially screen the negative ions on the PDMS surface, thereby decreasing the potential difference.

Taking the highest charge transfer value divided by the sample size as the maximum surface charge density that is achievable by ion injection, the increment in surface charge density was compared. Figure 1f shows the initial surface charge density that was fully generated by triboelectrification and the saturated surface charge density after multiple injection cycles for all the pristine and aged PDMS samples. The data revealed that the pristine PDMS sample trapped the most charges, represented by the highest gain in surface charge density, which almost doubled the original output. The 6-month-old PDMS film achieved an 11 µC m^{-2} increase in surface charge density, whereas the 17 month old film only showed a minor improvement, indicating a much poorer charge-trapping capability as the film ages.

2.2. Surface Work Function

To have a better understanding of the difference in charge generation between pristine and aged PDMS films, the contact potential difference (V_{CPD}) of these films were measured by Kelvin probe force microscopy (KPFM), which characterizes the work function of the sample surface as follows:

$$V_{CPD} = \frac{\phi_{tip} - \phi_{sample}}{-e} \qquad (1)$$

where ϕ_{tip} and ϕ_{sample} are work functions of the KPFM probe tip and the sample surface, respectively, and e is the charge of an electron.

Figure 2a shows the contact potential difference of all three samples with the biased tip voltage set to 3 V. With ageing, the V_{CPD} of PDMS films increased from -2.25 ± 0.18 to -2.02 ± 0.19 V and -1.74 ± 0.16 V after 6 months and 17 months, respectively,

ADVANCED
SCIENCE NEWS

www.advancedsciencenews.com

**ADVANCED
MATERIALS
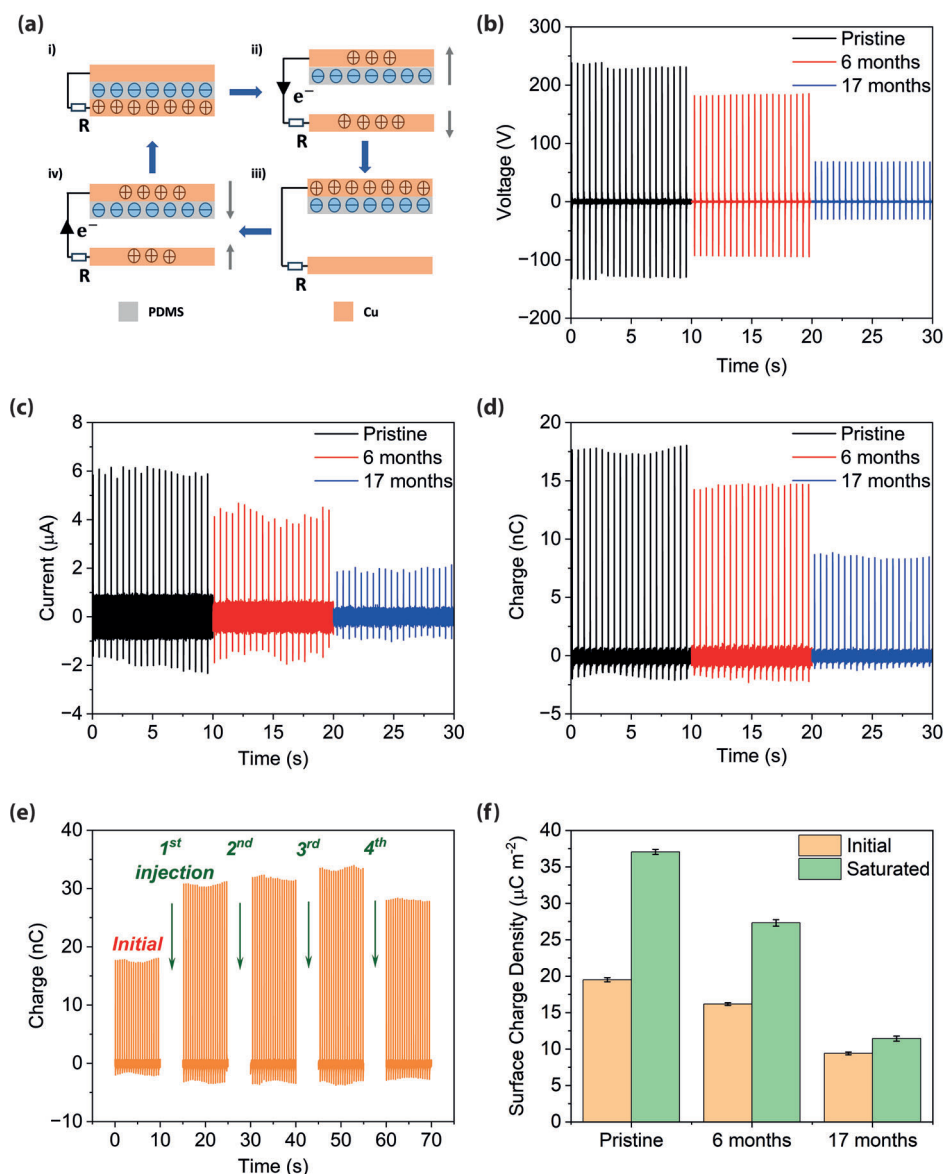INTERFACES**

www.advmatinterfaces.de

Figure 1. a) Schematic of the working principle of a conductor-to-dielectric contact-separation mode TENG. b–d) Comparison of the electrical output of pristine and aged PDMS-based TENGs, including open-circuit voltage, short-circuit current and charge transfer. e) Charge transfer in pristine PDMS-based TENG before and after injections of negative ions. f) Comparison of the initial and saturated charge transfer in pristine and aged PDMS-based TENGs.

indicating a decline in work function with ageing time. The work function quantifies the lowest thermodynamic energy required to remove an electron from a solid to a point in the vacuum and the effect of change in work function can be demonstrated by a surface states model, as illustrated in Figure 2b.[21] Initially, due to the difference in Fermi levels (E_F) between the contacting materials, upon contact, electrons on copper tend to hop into the PDMS surface to seek the lowest energy state. However, after ageing, the lowering of work function leads to an elevated Fermi level of the PDMS film, which decreases the energy gap between the PDMS film and copper. Consequently, less charge transfer is needed to balance the energy levels during contact. The lower energy gap hinders charge transfer from the copper to the PDMS surface,

thus reducing charge generation during contact electrification for the aged samples.

2.3. Surface Potential Profiles

To take a closer look at charge retention on these PDMS films, the evolution of surface potential was monitored to establish the history of surface charge decay. Assuming that the field from the charge to be neutralized extends exclusively through the dielectric film, the rate at which surface charge density σ decays as a function of time t can be described as follows:[22]

$$\sigma(t) = \sigma_0 \exp\left(-t/\tau_0\right) \tag{2}$$

ADVANCED
SCIENCE NEWS

www.advancedsciencenews.com

ADVANCED
MATERIALS
INTERFACES
Open Access
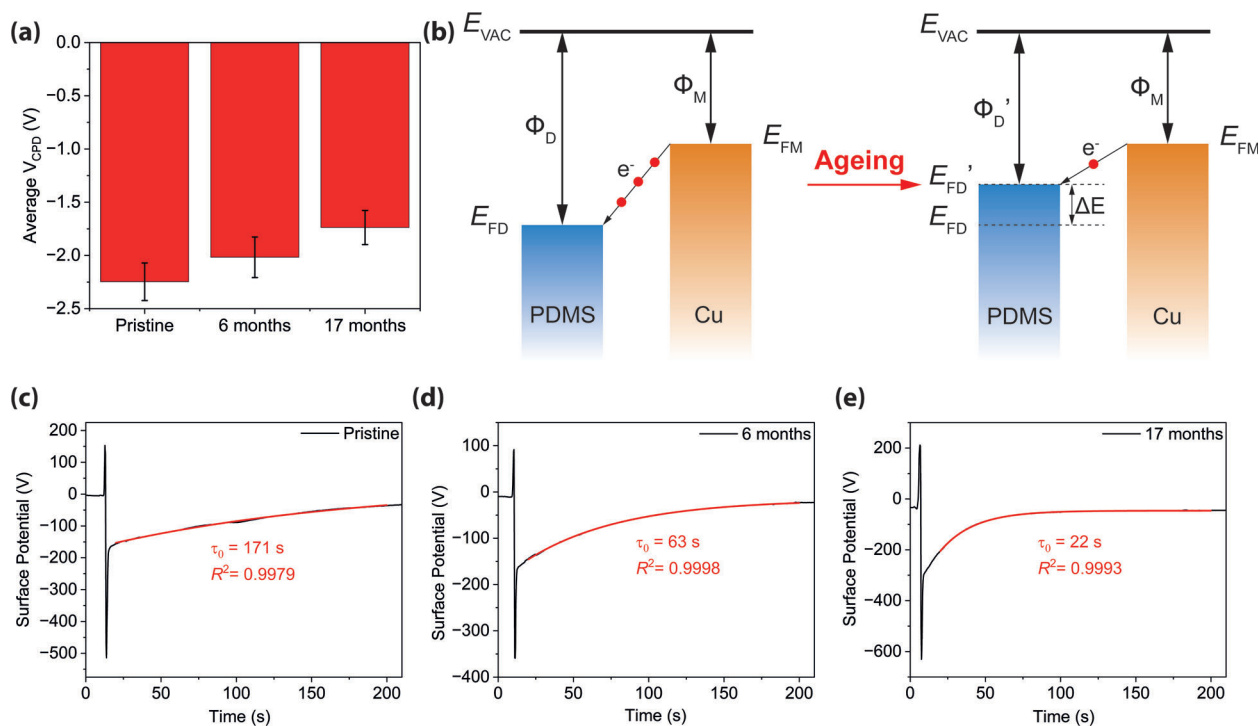
www.advmatinterfaces.de

Figure 2. a) Comparison of the average contact potential difference (CPD) between the tip and the pristine and aged PDMS samples. b) Surface states model for elucidating the charge transfer during contact electrification in the case of a metal-dielectric pair. E_{VAC}, vacuum level; E_{FD}, Fermi level of the dielectric; E_{FM}, Fermi level of the metal; ϕ_D and ϕ_D', work function of the dielectric before and after ageing; ϕ_M, work function of the metal. c–e) Surface potential profiles of the pristine and aged PDMS samples post injection of negative ions.

and

$$\tau_0 = \varepsilon \rho \tag{3}$$

where σ_0 is the initial surface charge density, τ_0 is the time constant, ε and ρ are the absolute permittivity and the bulk resistivity of the material, respectively.

Figure 2c–e shows the surface potential profile of all three samples after ion injection tests. Since surface potential is directly proportional to surface charge density, the profile should also follow the trend of an exponential decay. The time constant τ_0 from 20 to 200 s was therefore derived by fitting the curve to an exponential decay function of Equation (2). Our results suggest that the pristine PDMS film has the best charge retention performance, in that its charge decay curve has a time constant of $\tau_0 = 171$ s. Meanwhile, we found that the charge decays considerably faster for the other two samples, with the time constant being 63 s for the 6 month old sample, whereas only 22 s for the 17 month old sample.

2.4. Dielectric Properties

To better understand the difference in charge decay rate, the dielectric constant and impedance level of the three samples were measured, as shown in **Figure 3**a,b. The data indicate that the pristine PDMS film has the highest dielectric constant, which means that it can store more electric energy under the same electric field. Meanwhile, it also has the lowest electrical resis-

tance, which allows more charge to pass through when a certain voltage is applied. Compared to the pristine PDMS, the aged samples have relatively lower dielectric constant but higher bulk resistivity. At 0.001 MHz, the dielectric constant of the PDMS film fell from 3.5 to 2.9 after 17 months, but the bulk resistivity increased from 15 to 17 MΩ m. The evolution of these dielectric properties may be attributed to polymer degradation. Chemical decomposition processes like chain scission leads to deterioration of polymer chains and increased disorder of the underlying molecular structure, which results in decreased charge carrier mobility and restricted charge flow within the material.[23]

As derived in Equation (3), the time constant for charge decay is dependent on both permittivity and resistivity of the bulk material. With higher dielectric constant and higher resistivity, the surface charge on a material is expected to decay at a much lower rate. Despite having a lower resistivity, the dielectric constant of the pristine PDMS is significantly higher than the aged PDMS samples, the coupled effect of which makes the surface charge on the pristine PDMS film decay much slower.

Besides affecting the charge decay rate on the thin film, higher permittivity also enhances charge generation. For a conductor-dielectric type TENG in contact-separation mode, the open-circuit voltage across the two electrodes is given by:[24]

$$V_{oc} = \frac{\sigma x}{\varepsilon_0} \tag{4}$$

where x is the separation gap and $\varepsilon \epsilon_0$ is the permittivity of air.

**ADVANCED
SCIENCE NEWS**

www.advancedsciencenews.com

**ADVANCED
MATERIALS
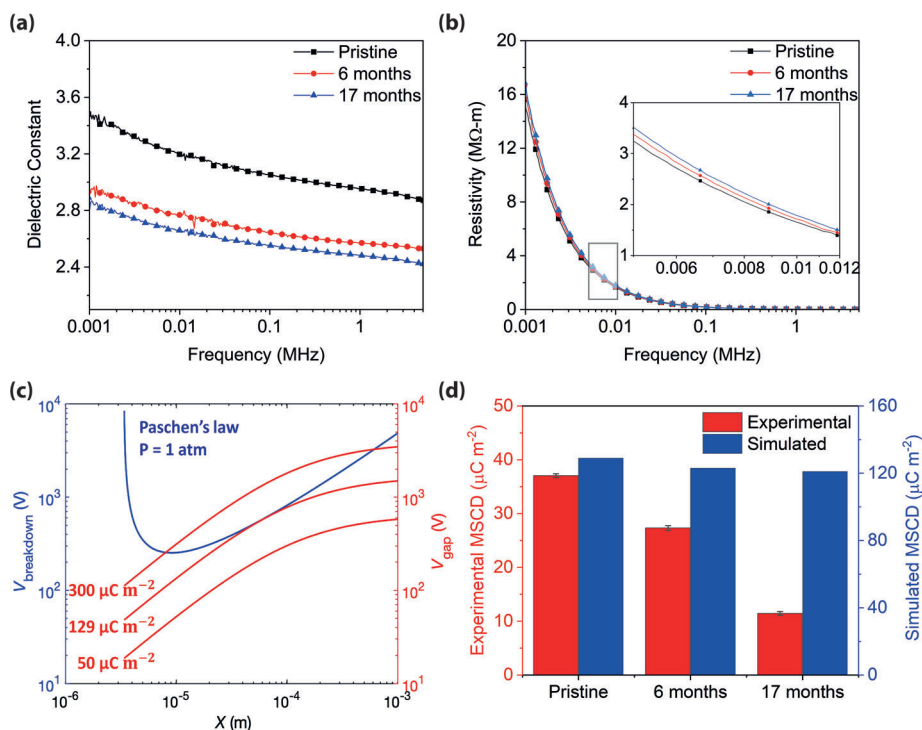INTERFACES**
Open Access

www.advmatinterfaces.de

Figure 3. a) Comparison of the dielectric constants of pristine and aged PDMS samples. b) Comparison of the bulk resistivity of pristine and aged PDMS samples. c) Analytical simulation of the relationship between the air breakdown voltage and the voltage drops across the air gap at surface charge densities of 50, 129, and 300 μC m⁻². d) Comparison of experimental and simulated maximum surface charge density on pristine and aged PDMS samples.

Considering the dielectric material as an ideal capacitor, the surface charge density σ that is generated from triboelectrification with copper can be expressed using the following equation:[25]

$$\sigma = 2\varepsilon_0 \varepsilon_r \left(\frac{\phi_M - \phi_D}{d} \right) \tag{5}$$

where ε_r is the dielectric constant of the dielectric material, ϕ_M and ϕ_D are work functions of the metallic and dielectric material respectively, and d is the thickness of the dielectric material.

From Equations (4) and (5), it is clear that with the same film thickness and work function difference, the output voltage is directly proportional to surface charge density, which scales linearly with dielectric constant. Aged samples with lower dielectric constant constrain the amount of triboelectric charge generated on the surface, hence leading to a poorer electrical performance than the pristine sample, which conforms with results shown in Figure 1b–d.

Moreover, the decrease in dielectric constant also limits the maximum surface charge density (MSCD) that is achievable on the surface. Since high voltage leads to air discharge, the MSCD on the dielectric film is mostly limited by the air breakdown effect. By Paschen's Law, the breakdown voltage can be described using the equation below:[26]

$$V_{breakdown} = \frac{A(Px)}{\ln(Px) + B} \tag{6}$$

where P is the air pressure, A and B are constants that are determined by the composition of pressure of the air.

At the same time, the magnitude of the voltage drop across the air gap between the contact surfaces under short-circuit condition can be expressed as follows:

$$V_{gap} = \frac{\sigma x d}{\varepsilon_0 (x\varepsilon_r + d)} \tag{7}$$

To prevent air discharge, the voltage drop across the air gap should always fall below the breakdown voltage, hence the following relationship needs to be satisfied at any separation distance:

$$\frac{A(Px)}{\ln(Px) + B} - \frac{\sigma x d}{\varepsilon_0 (x\varepsilon_r + d)} > 0 \tag{8}$$

From this relationship, we establish that the MSCD under certain ambient environment is given by:

$$\sigma_{max} = \left\{ \frac{AP\varepsilon_0 (x\varepsilon_r + d)}{d[\ln(Px) + B]} \right\}_{min} \tag{9}$$

To visualize the relationship between air breakdown and the surface charge density, analytical modelling was performed in MATLAB on the pristine PDMS film, as shown in Figure 3c. Below 129 μC m⁻², the voltage across the gap always falls below the breakdown voltage of air, delineating a safe region where the MSCD is not affected by the air breakdown effect. At
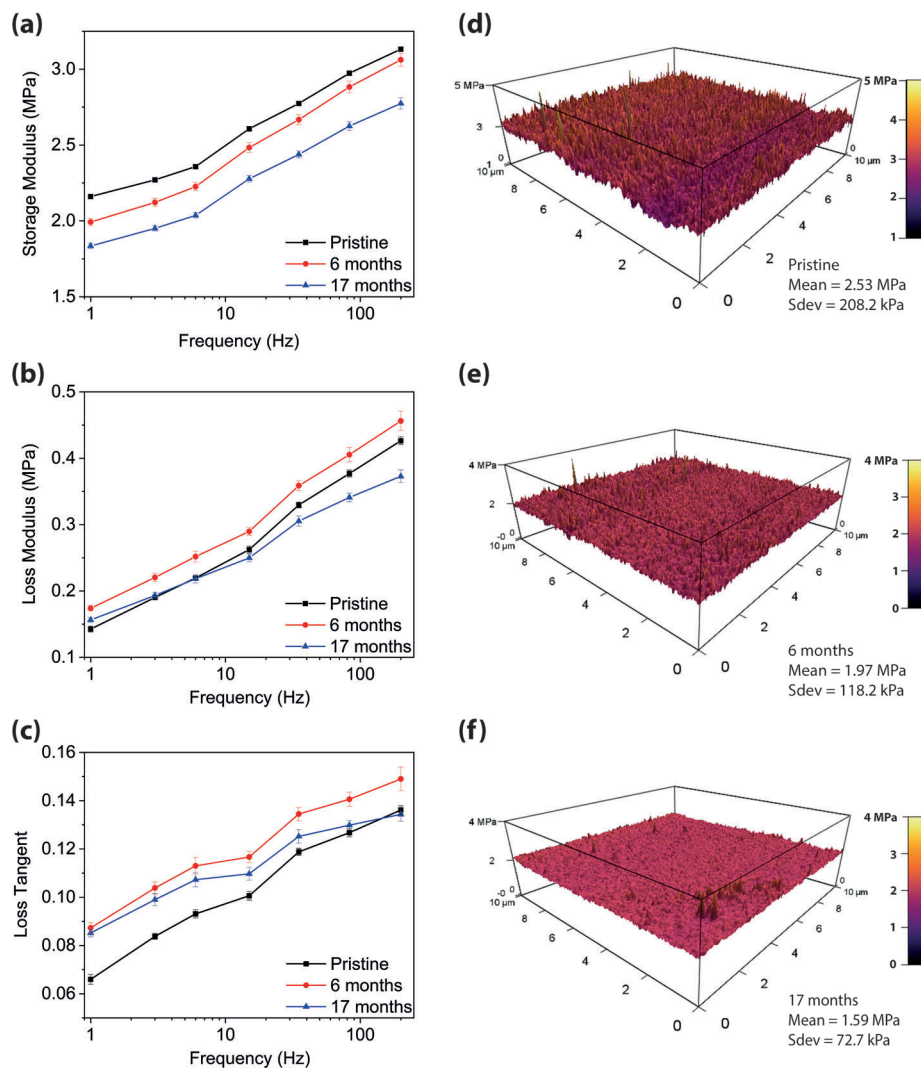
2400094 (5 of 10)

Figure 4. a–c) Comparison of the storage modulus (*E'*), loss modulus (*E''*), and loss tangent (*tan δ*) of the pristine and aged PDMS samples tested under DMA mode at frequencies between 1 and 200 Hz. d–f) Spatial variation of the Young's moduli measured on the surface of the pristine and aged PDMS samples via the AM-FM viscoelastic mapping technique.

129 µC m⁻², air breakdown voltage is reached at a separation gap of ca. 60 µm and the V_{gap} curve is in tangential contact with the $V_{breakdown}$ curve. Going further, surface charge density exceeds the threshold value, and the voltage across the gap will exceed the breakdown voltage of air, leading to air discharge and screening of the excess amount of surface charge. It can also be deduced from the model that air discharge can occur anywhere before the gap distance reaches 60 µm, which is well below the amplitude of displacement during TENG measurement, indicating the presence of air breakdown. Figure 3d compares the MSCD achievable on pristine and aged PDMS samples from predicted results. As the dielectric constant decreases with ageing, MSCD on PDMS also decreases, which conforms with the trend observed in Figure 1f. However, the predictions from the idealized analytical model are all well above the experimental results, which suggests that air breakdown might not be the only limiting factor that regulates the surface charge density. In addition, the measured surface charge density here is the surface charge

transferred as a result of the difference between the chemical potentials of the two contacting materials.[26] The experimental measure takes into account both the actual material properties and interactions at the interface, which differs from theoretical predictions.

2.5. Mechanical Properties

To study how changes in mechanical properties can affect the TENG performance, probe-based dynamic mechanical analysis (probeDMA) was performed to characterize the viscoelastic behavior of the pristine and aged PDMS samples. The storage modulus, loss modulus, and loss tangent of the viscoelastic samples are presented in **Figure 4a–c**. Compared to aged samples, pristine PDMS film has the highest storage modulus, which means the material is stiffer and more resistant to elastic deformation. Aged samples have a relatively lower storage modulus that we

ascribed to chain scission from chemical degradation, which not only limited their dielectric properties, but also lowered the overall degree of cross-linking within the sample.[27] The formation of short chains weakens the polymer and reduces its mechanical robustness. The difference in loss modulus of the PDMS samples is much smaller compared to that in storage modulus. By and large, the loss tangent of the pristine PDMS sample is lower than that of the aged samples, especially at low frequencies (typically 1–10 Hz) at which most TENGs operate. A smaller loss tangent contributes to less energy dissipation from viscoelastic effect during contact and separation, which allows for more mechanical energy to be converted to electrical energy under the same applied external force.

To push the detection limit even further, we employed the amplitude mode-frequency mode (AM-FM) from the Cypher AFM to perform surface viscoelastic mapping, which can reveal both the localized topographic and mechanical information of the sample surfaces at nanoscale resolution.[28] From the topography data, the pristine and aged samples are smooth and do not show significant difference in average surface roughness (Figure S7a–c, Supporting Information). In terms of mechanical properties, the Young's modulus data shown in Figure 4d–f are consistent with the probeDMA test results. The pristine PDMS sample manifested as the stiffest among the three and has the highest Young's modulus, with a mean value of 2.53 ± 0.21 MPa. With ageing, PDMS films get more compliant due to chemical degradation, with an average Young's modulus of 1.97 ± 0.12 and 1.59 ± 0.07 MPa, respectively, after 6 months and 17 months. It is also worth noting that the standard deviation of Young's modulus values is much higher for the pristine sample than the aged ones, which means that local stiffness values on the pristine PDMS film deviate more from the mean value. Heterogeneity in local surface stiffness can potentially contribute to more delocalized stress distribution across the sample area, which facilitates charge transfer between the contacting surfaces, and thereby enhances charge generation.[29]

In addition to viscoelastic properties, surface adhesion also plays a fundamental role in contact electrification. In our study, a pull-off test was performed to characterize the difference in adhesion between samples. A representative load-depth curve obtained from the pull-off test is illustrated in **Figure 5**. Regions where the load is positive indicate that the indenter tip is undergoing compression, whereas a negative load represents a tensile force. During the step of approaching, when the tip is close enough to the surface, the membrane snaps onto the tip due to adhesion, and a negative peak is observed at the point of contact ($\delta_{contact}$). This point is also regarded as the surface point, where the tip depth is defined as zero. Then loading starts at the prescribed rate until the maximum load is reached, followed by an unloading process occurring at the same rate. The hysteresis between the loading and unloading curves is mainly caused by energy dissipation from viscoelastic effects. Unloading continues until a sufficiently strong tensile force ($F_{pull-off}$) is reached at the pull-off point ($\delta_{pull-off}$) to detach the film from the tip, after which the tip is fully withdrawn from the sample surface. The shaded area under the load-depth (P–h) curve represents the total energy that is required to separate the tip from the sample at the interface during one loading cycle, which is denoted as the work of adhesion ($W_{adhesion}$).
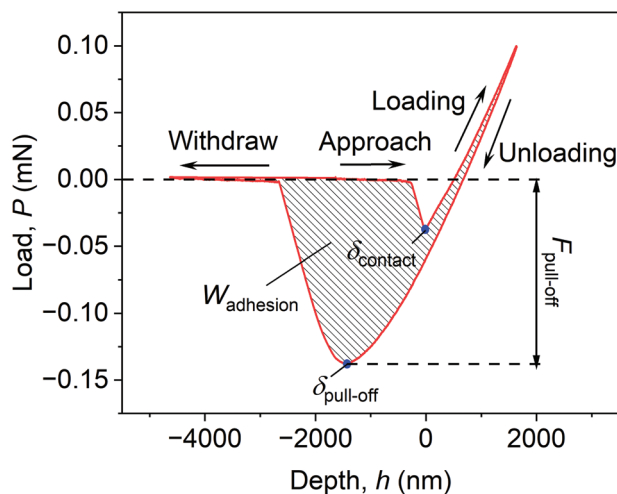

Figure 5. Representative example of a load-depth (P–h) curve during a pull-off test performed in a nanoindenter equipped with a flat-ended cylindrical probe (radius = 26 µm). $\delta_{contact}$ is the indentation depth at the jump-to-contact point. $\delta_{pull-off}$ and $F_{pull-off}$ are the indentation depth and the load at the point of maximum adhesive force, respectively. $W_{adhesion}$ is the work of adhesion incurred during one loading cycle, quantifiable by integrating the shaded area under the P–h curve.

Table 1 summarizes the pull-off force, pull-off stress, and the work of adhesion of the three samples. Results indicate that with ageing, the force required for sample detachment decreased, which means that the adhesive interaction between the tip and sample also diminished. The pristine PDMS film exhibits the highest adhesion among the three samples, with its pull-off stress at 30% and 40% higher than the 6 month old and 17 month old samples, respectively. The decline in adhesion can be a consequence of a loss in surface energy.[30] Reduction in bond strength and surface contamination lower the surface energy of aged samples, making the adhesive force between the contact surfaces weaker. A larger pull-off force would induce a higher detachment acceleration rate, which enhances the charge generation during separation, as indicated by the more negative peak values for the pristine PDMS sample shown in Figure 1b.[31] From an energy standpoint, a larger pull-off force allows the material to store more mechanical adhesion energy during a contact event, as evinced by the greater work of adhesion calculated from the area under the P–h curve (energy dissipated = $\oint P dh$), which further gets converted to extra triboelectric energy and increases the net electrical output.

Table 1. Comparison of the pull-off force, pull-off stress, and work of adhesion of pristine and aged PDMS samples. Pull-off force and pull-off stress values were averaged from 12 measurements. Work of adhesion values were calculated by integrating the area under the load-depth curve and averaged from 5 separate measurements.

Ageing condition	Pull-off force [mN]	Pull-off stress [MPa]	Work of adhesion [pJ]
Pristine	0.169 ± 0.004	0.080 ± 0.002	397 ± 11
6 months	0.132 ± 0.004	0.062 ± 0.002	264 ± 5
17 months	0.122 ± 0.008	0.057 ± 0.004	248 ± 15

**ADVANCED
SCIENCE NEWS**

www.advancedsciencenews.com

**ADVANCED
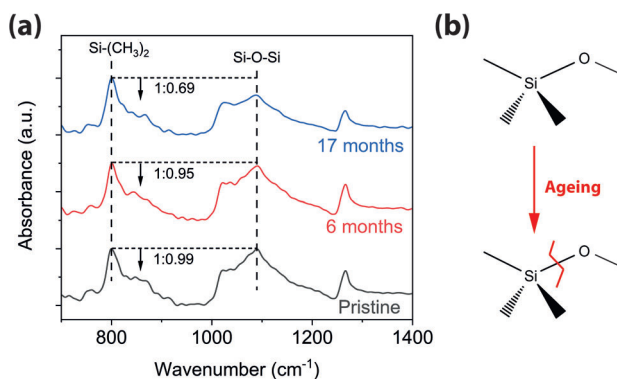MATERIALS
INTERFACES**
Open Access

www.advmatinterfaces.de

Figure 6. a) Comparison of the relative infrared peak intensity obtained from nano-FTIR spectra of the characteristic bands at 800 and 1091 cm^{-1} of the pristine and aged PDMS samples. b) Proposed mechanism by breakage of the Si—O bonds present on the surface of aged PDMS films.

2.6. Ageing Mechanism

To probe the ageing mechanism of the PDMS samples, we obtained nano-FTIR spectra from a scattering-type scanning nearfield optical microscope (s-SNOM) to reveal the local chemical information at a spatial resolution of ≈20 nm.[32] The average nano-FTIR spectra of pristine and aged PDMS samples obtained from a series of line scans (Figures S9–S11, Supporting Information) are shown in **Figure 6a**, with characteristic vibrational peaks matching the ATR-FTIR results (Figure S12, Supporting Information). From the nearfield spectra, we observe a change in relative intensity between the vibrational modes at 800 and 1091 cm,$^{-1}$ which are assigned to the Si–C stretching in the —Si—$(CH_3)_2$ groups and the Si–O stretching in the siloxane linkers (Si—O—Si), respectively.[33] With ageing, the stretching between Si and O atoms is suppressed, which suggests the presence of chain scission (Si–O bond breaking) associated with the ageing process of elastomers, as illustrated in Figure 6b. Interestingly, such a change in peak intensity was not obvious from the ATR-FTIR spectra, thereby supporting the notion that the proposed chain scission mechanism is predominantly a surface effect (as revealed by nano-FTIR), while the chemical composition of the bulk material has remained unchanged. Since chain scission is favored upon thermal ageing, we ascribe the ageing process more to the temperature variation in the environment, rather than photo-ageing from light exposure.[34]

3. Conclusions

To conclude, this study investigates the ageing effect of PDMS-based TENGs from both dielectric and mechanical standpoints, focusing on material evolution at the micro- and nanoscale. The ageing of PDMS leads to diminished charge generation and charge trapping abilities, as indicated by reduced electrical output, decreased maximum surface charge density, and accelerated surface charge decay. The dielectric property changes in aged PDMS samples are characterized by a lower dielectric constant but a higher resistivity. The changes in mechanical properties of aged samples are marked by a decrease in storage modulus and an increase in loss modulus and loss tangent determined at

low vibrational frequencies. At the nanoscale, ageing also renders the film surface less adhesive and less variable in its local stiffness. Chemically, ageing reduces the work function and induces chain scission within the polymer surface. The synergistic effect of these changes in properties significantly decreases TENG output.

In the light of these local property changes, potential solutions to ameliorate the ageing effect are suggested. To slow down the rate of chain scission reaction within the polymer, it will be advisable to store the films in a cool and dark environment where thermal- and photo-degradation can be mitigated. It is also recommended to incorporate functional fillers that can alter the dielectric and mechanical properties of the material, such as conducting fillers (e.g., graphene, carbon nanotubes or Ag/Au nanoparticles), fillers with high-k values (perovskites) and fillers with higher Young's modulus (e.g., SiO_2). It might also be possible to restore the electrical output by performing surface plasma treatment to functionalize the triboelectric surface and to enhance surface adhesion.

This work gives valuable insights into the ageing problem potentially faced by PDMS-based TENGs and paves way for future research to investigate the ageing effect of other types of polymers adopting a similar approach. We hope the results will stimulate future research to mitigate these adverse effects associated with elastomeric triboelectric devices.

4. Experimental Section

Materials: All chemicals used in this work are commercially available. Sylgard 184 (PDMS elastomer and curing agent) was obtained from Dow Corning.

Preparation of Pristine and Aged PDMS: First, the PDMS base solution and curing agent was thoroughly mixed at a weight ratio of 10:1. After fully degassed in a vacuum desiccator, the mixture was casted onto a clean glass substrate using a doctor-blade with a fixed gap distance to obtain films with a uniform thickness. The film was then cured in the oven at 90 °C for 2 h. The two aged samples were prepared by leaving the PDMS films in an unsealed container stored in the cabinet under ambient conditions for 6 months and 17 months, respectively. The average thickness of the prepared films was determined to be 0.41 ± 0.07 mm.

Fabrication of PDMS/Cu TENG: The TENG devices were tested in a contact-separation mode, see Figure S1 (Supporting Information). The as-fabricated PDMS films were adhered onto conductive copper (Cu) tapes with adhesives on both sides and used as the negative electrification layer. The copper tapes served as electrodes and were directly attached to an insulating polyethylene terephthalate (PET) substrate to avoid charge loss. On the positive side, copper sheets were pasted onto another PET substrate and used as both the electrification material and the electrode. Copper wires were attached to both electrodes via Cu tapes. To achieve full contact, soft rubber sheets were placed underneath the PET substrates as buffer layers. The nominal contact area of the device is 3×3 cm^2.

TENG Measurements: All TENG measurements were carried out on a customized contact–separation test rig, with the cyclic loading controlled by a power supply, a function generator, and a magnetic shaker. In a standard test, the peak-to-peak amplitude of displacement is kept constant at 1.5 mm. The tapping frequency is at 2 Hz and the tapping force is maintained at roughly 60 N determined by a load cell. The output voltage was recorded on an oscilloscope (Picoscope 5442D) with a 100 MΩ high voltage probe (Rigol RP1300H). The output current and charge transfer were both measured by an electrometer (Keithley 6514).

Materials Characterization: The surface features of the PDMS films were examined under a scanning electron microscope (Hitachi

TM3030Plus SEM). The work functions were characterized using the Kelvin probe force microscopy (KPFM) mode in an atomic force microscope (Oxford Instruments Cypher-ES AFM). In KPFM measurements, samples were wiped clean with iso-propanol and left discharged overnight before placed onto a silicon wafer. An electrically conductive AFM probe was deployed to scan an area of 100 µm² at a scan rate of 0.75 Hz and the probe tip was driven electrically at a bias voltage of 3 V. The DC voltage applied to negate the tip oscillation during contact was recorded as the potential difference between the tip and the sample surface. The surface charge decay rate was determined from the surface potential profile obtained from a surface direct current (DC) voltmeter (AlphaLab USSVM2). The dielectric measurements were performed on an inductance-capacitance-resistance (LCR) meter (Hioki IM3536) with frequencies ranging from 4 Hz to 5 MHz, which follow the ones reported in literature.[35] The viscoelastic and adhesion properties were measured by a nanoindenter (iMicro KLA Tencor). The viscoelastic mapping was performed using the amplitude mode-frequency mode (AM-FM) in Cypher-ES AFM.[28] In this mode, the cantilever is simultaneously driven at two different mechanical resonances. The amplitude mode (AM) keeps the cantilever amplitude constant and gives topographic feedback and informs on dissipation within the material, while the frequency mode (FM) adjusts the drive frequency to give mechanical response, which measures stiffness variation of the sample.[29] A standard AFM probe was used to scan a sample area of 100 µm² at a scan rate of 1 Hz. The tip geometry was set to a Hertz cylindrical punch and the tip radius was fixed at 1.21 µm to match the measured Young's modulus of a reference sample, from which Young's moduli of other samples were derived. The Fourier-transform infrared (FTIR) spectra were recorded by a Nicolet iS10 FTIR spectrometer equipped with an attenuated total reflectance (ATR) module. The nano-FTIR spectra were obtained from a scattering-type scanning nearfield optical microscope (Neaspec s-SNOM), where a platinum-coated cantilever tip operating at its mechanical resonance frequency (273 kHz) was illuminated by an IR laser source covering the range from 700 to 1400 cm⁻¹.[32] Interferometric detection transforms the optical response into a complex-valued near-field signal, whose real part and imaginary part refer to the nano-FTIR reflectance and absorption spectrum, respectively. Each spectrum was acquired from an average of 11 Fourier-processed interferograms with 6.228 cm⁻¹ spectral resolution, 1024 points per interferogram, and 12 ms integration time per pixel. The sample spectrum was normalized to a reference spectrum measured on the silicon substrate. All measurements were carried out under ambient conditions.

Ion Injection Test: Maximum surface charge density (MSCD) is an important parameter that characterizes the charge trapping ability of the films, and it is usually not achievable from the triboelectrification process alone, where the surface charge is limited by the surface potential difference between the contacting materials. To reach MSCD the film can hold, an ion injection test was performed to artificially induce polarized ions onto the membrane surface, as reported in the literature.[26] An antistatic gun (MILTYPRO Zerostat3) was used in the test, which can generate charged ions of both polarities by triggering the discharge of air inside, and the polarity of injected ions can be manually controlled through squeezing and releasing of the trigger bar. In the test, the trigger was first squeezed with the outlet of the gun facing away from the membrane surface to release all the positive charges. Subsequently, the trigger was gently released after positioning the outlet of the gun straight towards the film surface with a horizontal distance of 1 in., during which negative ions were released and accumulated on the target surface. By grounding the back electrode attached to the film, injected negative ions electrostatically induced the same amount of electron transfer from the electrode to the ground, which led to a positive charge of equal density at the bottom surface of the sample.

Surface Potential Profiling: An antistatic gun was adopted in surface potential profiling to introduce negative ions onto the sample surface. All PDMS films rested on a grounded copper pad with an area much larger than the film size, which ensured that most charges would move through the interior of the bulk material.[19,22] Before injection, the films were placed under ambient conditions overnight to dissipate all the sur-

face charges. During the test, one stroke of negative ions was injected onto the membrane surface and the voltmeter probe clamped 1 in. above continuously recorded the real-time surface potential variation for 4 mi until a plateau was reached at charge screening.

Dynamic Mechanical Analysis: Probe-based dynamic mechanical analysis (probeDMA) was performed implementing the technique developed for the KLA nanoindenter.[36] A flat-ended diamond cylindrical punch (radius = 26 µm) was used to apply an oscillating stress on the sample at varying frequency, and the resultant displacement oscillation was recorded to reveal information about the storage modulus, loss modulus and the loss tangent of the viscoelastic sample. The storage modulus (E') is a measure of stored energy under deformation and quantifies the elastic property of the sample. On the other hand, the loss modulus (E'') quantifies the viscous response, and it measures energy dissipation during a loading cycle. The ratio of loss modulus and storage modulus gives the loss tangent ($\tan \delta = E''/E'$), which characterizes damping in the material. A total of 12 tests were performed in 3 discrete regions on a 1×1 cm² sample area, and 4 points were selected in each region.

Pull-Off Adhesion Test: Pull-off tests were performed based on experimental procedures employing the nanoindenter, as reported in literature.[37] During the pull-off test, a cylindrical flat punch with a radius of 26 µm was initially withdrawn 2 µm from the sample surface, ensuring that the tip was fully out of the adhesion interaction zone. The tip then started approaching at a speed of 100 nm s⁻¹ until it was in vicinity of the surface. To allow more accurate surface detection, the phase signal was monitored in this process until a phase change larger than 15° was detected. After contacting the surface, an indent was performed at a loading rate of 0.01 mN s⁻¹ to a maximum load of 0.1 µN. The tip was held in peak load position for 2 s before it was unloaded at the same rate, and eventually withdrawn 5 µm from the sample surface. The nominal pull-off stress is determined by dividing the pull-off force by the contact area of the flat-ended punch (area = 2124 µm²). The work of adhesion is determined by calculating the enclosed area established under the load-depth curve. A total of 12 tests were performed in 3 discrete regions on a 1×1 cm² sample area, and 4 points were selected in each region.

Supporting Information

Supporting Information is available from the Wiley Online Library or from the author.

Conflict of Interest

The authors declare no conflict of interest.

Data Availability Statement

The data that support the findings of this study are available from the corresponding author upon reasonable request.

[1] I. Miranda, A. Souza, P. Sousa, J. Ribeiro, E. M. S. Castanheira, R. Lima, G. Minas, *J. Funct. Biomater.* **2021**, *13*, 2.

[2] X. Tao, X. Chen, Z. L. Wang, *Energy Environ. Sci.* **2023**, *16*, 3654.

[3] J. Ye, J.-C. Tan, *Nano Energy* **2023**, *114*, 108687.

[4] M. S. U. Rasel, J.-Y. Park, *Appl. Energy* **2017**, *206*, 150.

[5] A. Kaur, A. Gupta, C. Ying, M. Rahmani, G. Sapra, *Microelectron. Eng.* **2023**, *275*, 111992.

[6] W. Li, L. Lu, A. G. P. Kottapalli, Y. Pei, *Nano Energy* **2022**, *95*, 107018.

[7] I. Domingos, Z. Saadi, K. S. Sadanandan, H. A. Pocinho, D. M. Caetano, A. I. S. Neves, M. F. Craciun, H. Alves, *Nano Energy* **2023**, *115*, 108688.

[8] J. Li, C. Wu, I. Dharmasena, X. Ni, Z. Wang, H. Shen, S.-L. Huang, W. Ding, *Intell. Converged Networks* **2020**, *1*, 115.

[9] W. Zhang, Y. Xi, E. Wang, X. Qu, Y. Yang, Y. Fan, B. Shi, Z. Li, *ACS Appl. Mater. Interfaces* **2022**, *14*, 20122.

[10] J. Chen, K. Han, J. Luo, L. Xu, W. Tang, Z. L. Wang, *Nano Energy* **2020**, *77*, 105171.

[11] H. Kang, C. Zhao, J. Huang, D. H. Ho, Y. T. Megra, J. W. Suk, J. Sun, Z. L. Wang, Q. Sun, J. H. Cho, *Adv. Funct. Mater.* **2019**, *29*, 1903580.

[12] Q.-J. Sun, Y. Lei, X.-H. Zhao, J. Han, R. Cao, J. Zhang, W. Wu, H. Heidari, W.-J. Li, Q. Sun, V. A. L. Roy, *Nano Energy* **2021**, *80*, 105521.

[13] S. Vlassov, S. Oras, M. Antsov, I. Sosnin, B. Polyakov, A. Shutka, M. Y. Krauchanka, L. M. Dorogin, *Rev. Adv. Mater. Sci.* **2018**, *56*, 62.

[14] Y.-M. Wang, X. Zhang, C. Liu, L. Wu, J. Zhang, T. Lei, Y. Wang, X.-B. Yin, R. Yang, *Nano Energy* **2023**, *107*, 108149.

[15] Y. Gao, G. Yu, J. Tan, F. Xuan, *Sens. Actuators, A* **2018**, *280*, 205.

[16] L. Ģērmane, L. Lapčinskis, M. Iesalnieks, A. Šutka, *Mater. Adv.* **2023**, *4*, 875.

[17] J. Seo, S. Hajra, M. Sahu, H. J. Kim, *Mater. Lett.* **2021**, *304*, 130674.

[18] Y. S. Choi, S. W. Kim, S. Kar-Narayan, *Adv. Energy Mater.* **2021**, *11*, 2003802.

[19] J. Zhao, Y. Shi, *Adv. Funct. Mater.* **2023**, *33*, 2213407.

[20] Y. Liu, W. Liu, Z. Wang, W. He, Q. Tang, Y. Xi, X. Wang, H. Guo, C. Hu, *Nat. Commun.* **2020**, *11*, 1599.

[21] C. Xu, Y. Zi, A. C. Wang, H. Zou, Y. Dai, X. He, P. Wang, Y. C. Wang, P. Feng, D. Li, Z. L. Wang, *Adv. Mater.* **2018**, *30*, 1706790.

[22] N. Jonassen, in *Electrostatics 2nd Edition*, Springer, US, Boston, MA **2002**, pp. 41–59.

[23] C. Van Dyck, T. J. Marks, M. A. Ratner, *ACS Nano* **2017**, *11*, 5970.

[24] S. Niu, S. Wang, L. Lin, Y. Liu, Y. S. Zhou, Y. Hu, Z. L. Wang, *Energy Environ. Sci.* **2013**, *6*, 3576.

[25] S. Paria, S. K. Si, S. K. Karan, A. K. Das, A. Maitra, R. Bera, L. Halder, A. Bera, A. De, B. B. Khatua, *J. Mater. Chem. A* **2019**, *7*, 3979.

[26] S. Wang, Y. Xie, S. Niu, L. Lin, C. Liu, Y. S. Zhou, Z. L. Wang, *Adv. Mater.* **2014**, *26*, 6720.

[27] C. Jin, Z. Wang, A. A. Volinsky, A. Sharfeddin, N. D. Gallant, *Polym. Test.* **2016**, *56*, 329.

[28] G. Lamour, C. K. Yip, H. Li, J. Gsponer, *ACS Nano* **2014**, *8*, 3851.

[29] A. Šutka, L. Lapčinskis, O. Verners, L. Ģērmane, A. Smits, A. Pludons, S. Gaidukovs, I. Jerāne, M. Zubkins, K. Pudzs, P. C. Sherrell, J. Blums, *Adv. Mater. Technol.* **2022**, *7*, 2200162.

[30] J. H. Lee, I. Yu, S. Hyun, J. K. Kim, U. Jeong, *Nano Energy* **2017**, *34*, 233.

[31] A. H. Ibrahim, P. F. Dunn, R. M. Brach, *J. Aerosol Sci.* **2003**, *34*, 765.

[32] A. F. Moslein, M. Gutierrez, B. Cohen, J. C. Tan, *Nano Lett.* **2020**, *20*, 7446.

[33] L. M. Johnson, L. Gao, C. W. Shields IV, M. Smith, K. Efimenko, K. Cushing, J. Genzer, G. P. López, *J. Nanobiotechnol.* **2013**, *11*, 22.

[34] N. S. Tomer, F. Delor-Jestin, L. Frezet, J. Lacoste, *Open J. Org. Polym. Mater.* **2012**, *02*, 13.

[35] A. S. Babal, A. K. Chaudhari, H. H. M. Yeung, J. C. Tan, *Adv. Mater. Interfaces* **2020**, *7*, 2000408.

[36] J. Hay, E. Herbert, *Exp. Tech.* **2013**, *37*, 55.

[37] D. M. Ebenstein, *J. Mater. Res.* **2011**, *26*, 1026.